



# An experimental and theoretical validation of dual role of Fe on improving the photocatalytic performance of doped mixed phase titania



S.K. Nikhil<sup>a</sup>, Gopika Rajeev Nair<sup>a</sup>, Abinash Das<sup>b</sup>, Sebin Devasia<sup>b</sup>, Ranjith G. Nair<sup>a,\*</sup>

<sup>a</sup> Solar Energy Materials Research and Testing Laboratory, Department of Physics, National Institute of Technology Silchar, Silchar, Assam 788010, India

<sup>b</sup> PSG Institute of Advanced Studies, Coimbatore, Tamil Nadu 641004, India

## ARTICLE INFO

### Article history:

Received 16 April 2024

Received in revised form 13 August 2024

Accepted 23 September 2024

### Keywords:

Photocatalysis

Direct Z-Scheme

TiO<sub>2</sub>

Phase transformation

Doping

## ABSTRACT

The present work proposes a strategic approach of using Fe doping to form a mixed-phase TiO<sub>2</sub> direct Z-scheme catalyst at low onset temperature. The doping-induced modifications are explained from the experimental and theoretical viewpoint. Fe-doped Z-scheme-based mixed-phase TiO<sub>2</sub> at optimal calcination temperature (TiFe-400) exhibits maximum photon absorption and reduces charge carrier recombination, enhancing photocatalytic and PEC performance. TiFe-400 has the highest rate constant for the degradation of MB (0.084 min<sup>-1</sup> under solar irradiation) and showed exceptional photooxidation current (0.8 mA, 1.3 V vs Ag/AgCl). The Z-scheme formation significantly inhibits the recombination of photocarriers, resulting in a directed migration of charge carriers to the high redox potential mixed-phase TiO<sub>2</sub>. This migration is validated by identifying the primary reactive species participating in the photocatalytic process. This work, demonstrating both experimental and theoretical approaches, may provide valuable insight into designing stable and inexpensive catalysts for dual applications on an industrial scale.

© 2024 The Society of Powder Technology Japan. Published by Elsevier BV and The Society of Powder Technology Japan. All rights are reserved, including those for text and data mining, AI training, and similar technologies.

## 1. Introduction

Solar energy utilisation in addressing environmental and energy issues is one of the current focuses of the paradigm. Among all oxide-based photoactive materials, TiO<sub>2</sub> has been considered an ideal choice for photoelectrochemical (PEC) water-splitting and photocatalytic applications. Despite this, the efficacy of TiO<sub>2</sub> is constrained due to its band gap energy and the significant photoinduced charge carrier recombination rate [1,2]. Attempts were undertaken to broaden the absorption spectrum and effective charge carrier separation to increase the performance of TiO<sub>2</sub> as a catalyst. Given this, several techniques, such as the formation of heterojunctions, doping with metal/non-metals, sensitisation with noble metals, etc., have been identified, which are found to improve the physical, chemical and optical properties of TiO<sub>2</sub>.

The formation of type-II heterojunction with suitable semiconductors has been a proven strategy to improve the performance of photocatalysts through effective charge carrier separation at the interface [3,4]. However, this strategy has the disadvantage of using complex synthesis routes, and the heterojunctions thus

formed are found to have an issue of instability [5]. However, different polymorphs of TiO<sub>2</sub> allow the formation of junctions between the polymorphs without involving other catalyst support, which is very simple from an experimental standpoint. Among the possible mixed phase junction between the TiO<sub>2</sub> polymorphs, the anatase–rutile phase junction effectively improves the charge carrier separation via an internal electric field [6,7]. Numerous studies have been reported explaining the charge transfer mechanisms and the photocatalytic and water-splitting applications of mixed-phase TiO<sub>2</sub> [8,9]. The nature of heterojunction formed in mixed-phase TiO<sub>2</sub> is found to be type-II in most of the reported works, which minimises the redox ability of the material due to the accumulation of photoinduced charge carriers at low redox potential band edges of respective semiconductors [10]. However, some studies have shown a possibility of direct Z-scheme formation in mixed-phase TiO<sub>2</sub> [11,12]. While the direct Z-scheme and Type-II heterojunctions have comparable energy band arrangements, the distinctive charge transfer mechanism in direct Z-scheme allows better charge separation and redox ability [13]. However, along with direct Z-scheme formation, suitable optical modifications are required to improve the absorption capacity of mixed-phase TiO<sub>2</sub>, making it more efficient from an application outlook. In addition, the formation of mixed-phase TiO<sub>2</sub> requires high thermal

\* Corresponding author.

E-mail address: [rgnair@phy.nits.ac.in](mailto:rgnair@phy.nits.ac.in) (R.G. Nair).

treatment ( $>600$  °C), which is another constraint for large-scale usage. Until now, researchers mostly employ calcination to attain phase transformation (anatase to rutile). To our knowledge, reports on doping-induced mixed phase formation are minimal, which will reduce the onset temperature for phase transformation to a considerable limit. Moreover, selecting a suitable dopant will also lessen the forbidden energy gap.

In addition to excellent charge transport properties, a photocatalyst should also have suitable absorption capacity for efficient photon harvesting. Doping  $\text{TiO}_2$  with suitable dopants (metals/non-metals) is found to tune the band gap for efficient photon harvesting [14]. In this regard, studies have shown that doping  $\text{TiO}_2$  with transition metal shifts the absorption towards higher wavelengths [15,16]. Soni et al. doped anatase  $\text{TiO}_2$  with 04 different transition metals and studied their performance in water pollution treatment [17]. They explained the better performance of the doped  $\text{TiO}_2$  based on improvement brought about in the physicochemical properties of  $\text{TiO}_2$  after doping. Among variously reported transition metal ions-based dopants, Iron ( $\text{Fe}^{3+}$ ) is the favoured one due to its similar ionic radius with  $\text{Ti}^{4+}$  and its ability to enhance hydroxyl radical formation [18–20]. However, it is observed that a higher concentration of Fe may cause detrimental effects on the physicochemical properties of the modified material. At lower Fe concentrations, the induced impurity trap sites act as charge separators and transfer mediators. Still, a higher dopant concentration may lead the same trap sites to behave as recombination centres [21]. Moreover, experimental studies alone are insufficient to provide detailed insight into the optical and electronic of Fe-modified  $\text{TiO}_2$ . Theoretical investigation on the interaction of  $\text{TiO}_2$  and Fe using density functional theory (DFT) can complement the experimental outcomes to show the origin and trend of modified properties of anatase  $\text{TiO}_2$  after Fe doping.

In the present work, we aim to understand the effect of Fe-doped  $\text{TiO}_2$  on photocatalytic and PEC performance by evaluating the modified physicochemical and optical properties in a unified theoretical and experimental system. The present work utilizes Fe doping as an effective strategy to reduce the onset temperature

for forming mixed-phase  $\text{TiO}_2$ , thereby achieving direct Z-scheme heterojunction to address the absorption ability and recombination loss. As per the authors' knowledge, works reported in this direction are less explored. Fe-doped  $\text{TiO}_2$  synthesised via sol-gel method are subjected to various experimental and theoretical analyses to understand the material's modified electronic, optical and physicochemical properties. In light of this, a possible mechanism for enhanced performance was proposed and discussed based on an electrochemical and radical trapping study.

## 2. Materials and methods

### 2.1. Materials

Analytical grade precursors and solvents were used in the synthesis and testing processes. Titanium isopropoxide ( $\text{TiC}_{12}\text{H}_{28}\text{O}_4$ ), Iron(III)nitrate nonahydrate ( $\text{Fe}(\text{NO}_3)_3 \cdot 9\text{H}_2\text{O}$ ), ethanol, hydrochloric acid (HCl, 36 %) and probe pollutants were purchased from Sigma-Aldrich and were of the highest purity. Double-distilled Millipore water was used throughout the synthesis process.

### 2.2. Synthesis of Fe-doped $\text{TiO}_2$

The doped and undoped  $\text{TiO}_2$  samples were synthesised using an ultrasonication-assisted sol-gel method, as reported in our previous work [22]. First, 2 ml of titanium isopropoxide was added to 10 ml of ethanol and stirred magnetically for 1 hr, followed by 30 min ultrasonication. Later, Iron (III) nitrate nonahydrate with the required amount for 0.1 % Fe doping was added to the solution. Simultaneously, 5 M HCl (4 ml) and ethanol (10 ml) were added dropwise to the resultant solution under continuous stirring until gel formed. The sample was dried at 100 °C for 12 hrs in a hot air oven and further ground to a fine powder using mortar-pestle. The powder sample was calcined in air using a muffle furnace at calcination temperatures 300 °C, 400 °C, 500 °C, 600 °C and 625 °C respectively, with a ramping rate of 4 °C/min for 1 h.

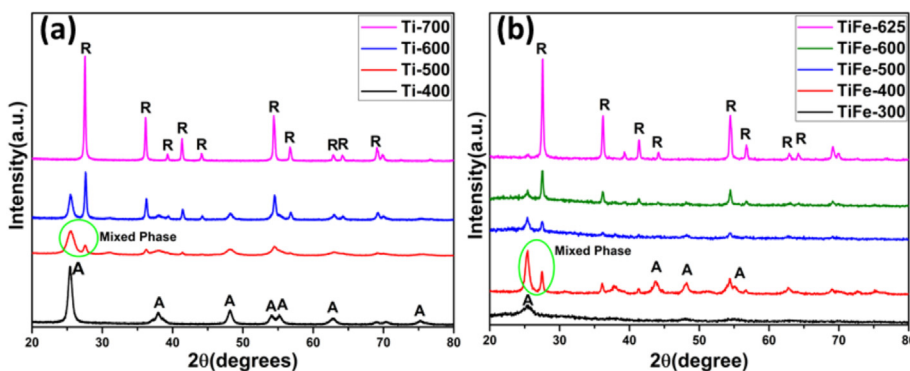


**Fig. 1.** XRD pattern of (a) undoped  $\text{TiO}_2$ , (b) doped  $\text{TiO}_2$  under different calcination temperature.

**Table 1**  
Crystallographic parameters of the samples.

Sample	Percentage Composition (%)		Crystallite Size(nm)			A/R Ratio
	Anatase	Rutile	Anatase	Rutile	Average Crystallite Size	
<b>Ti-400</b>	100	—			17.57	—
<b>TiFe-300</b>	100	—	5.06	—	5.06	—
<b>TiFe-400</b>	60	40	15.24	26.06	20.65	1.48
<b>TiFe-500</b>	48	52	27.11	29.94	28.88	1.06
<b>TiFe-600</b>	28	72	27.85	31.07	30.35	0.37
<b>TiFe-625</b>	—	100	—	32.67	32.67	—

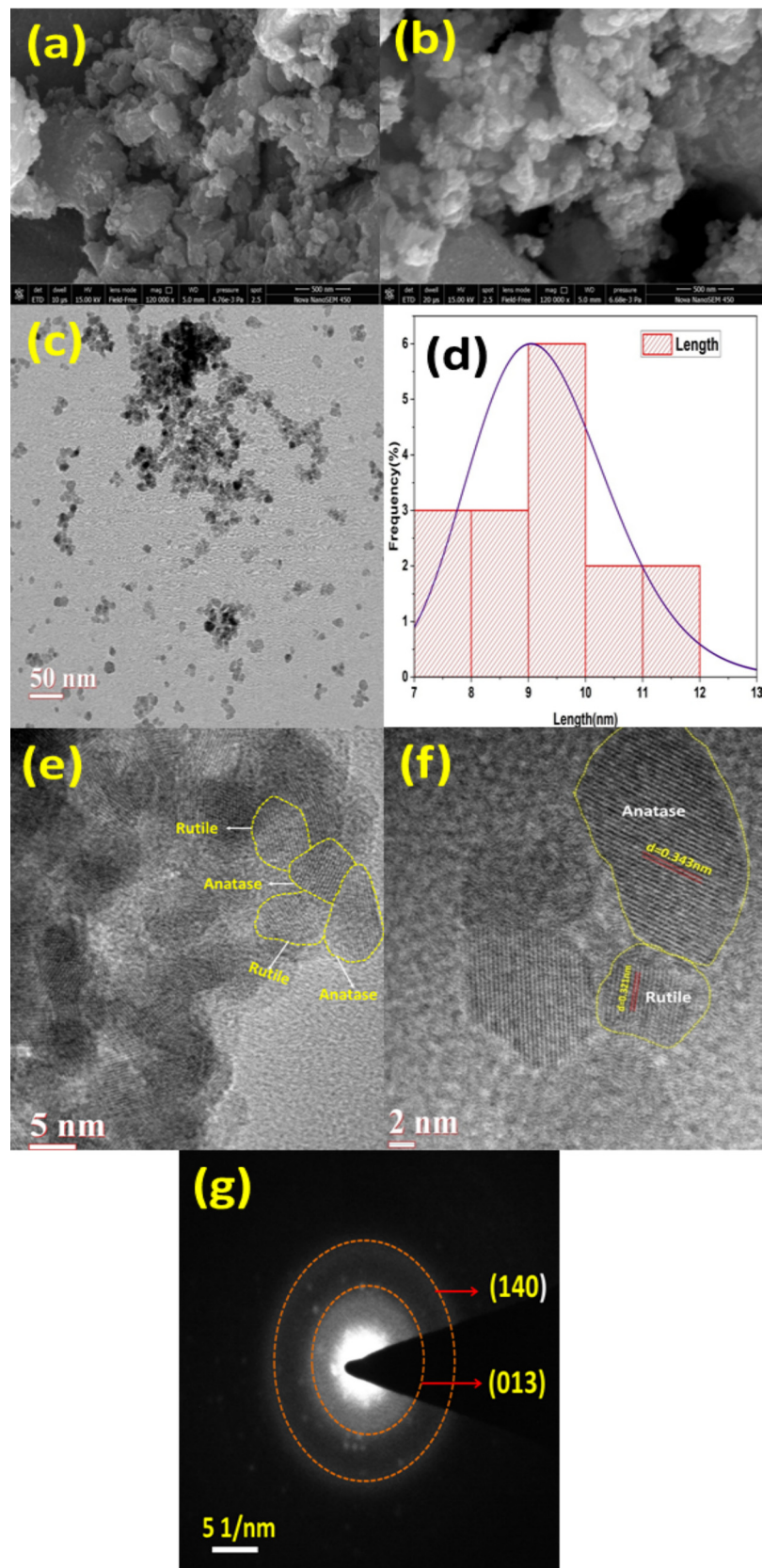


**Fig. 2.** FESEM images of (a)Ti-400,(b)TiFe-400, (c)TEM image,(d) Particle size distribution histogram (e-f) HRTEM image and (f) SAED pattern of TiFe-400.

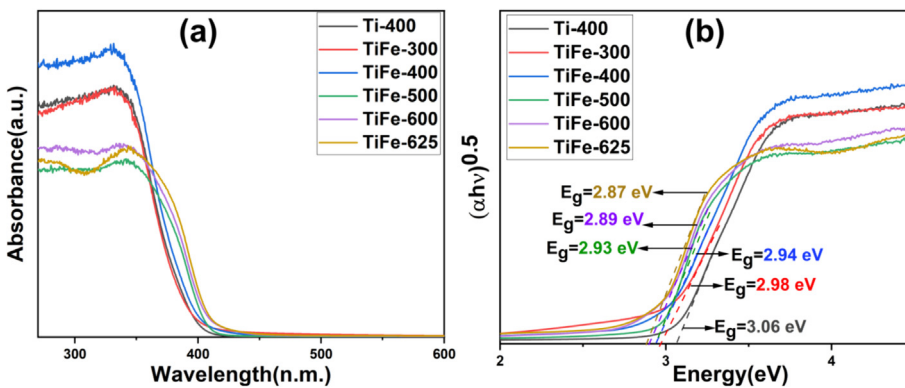


**Fig. 3.** (a) Absorption spectra,(b) Tauc's plot of the samples.

**Table 2**

Bandgap, charge transfer resistance and rate constant values of the samples.

Sample	Bandgap (eV)	$R_{ct}$ ( $\Omega$ )	Rate Constant( $\times 10^{-2} \text{ min}^{-1}$ )			
			Solar irradiation		Visible Irradiation	
			M.B	M.Y	M.B	M.Y
Ti-400	3.06	—	4.72	0.58	0.50	0.70
TiFe-300	2.98	185.90	0.41	0.60	0.83	1.23
TiFe-400	2.94	6.87	7.63	8.41	2.35	7.29
TiFe-500	2.93	180.27	5.20	6.20	1.04	4.37
TiFe-600	2.89	349.07	3.74	2.41	0.92	3.07
TiFe-625	2.87	479.00	0.12	0.93	0.65	2.37

The final samples were labelled as TiFe-300, TiFe-400, TiFe-500, TiFe-600 and TiFe-625 by their calcination temperature. A similar approach is adopted to prepare undoped  $\text{TiO}_2$  except for the usage of Iron (III) nitrate nonahydrate and calcined at 400 °C, 500 °C, 600 °C, and 700 °C and is denoted as Ti-400, Ti-500, Ti-600 and Ti-700.

### 2.3. Characterization

#### 2.3.1. Structural and optical characterizations

The structural properties of the samples were analysed using a PANalytical X-ray powder diffractometer(Model: Xpert3 Powder, Cu  $K_{\alpha 1}$  source). Field Emission Scanning Electron Microscopy (FESEM) analyses were done to understand the surface morphology using a Nova Nano FE-SEM 450 (FEI). The absorbance and photoluminescence analyses of the samples were carried out using Agilent make (Model: Cary 5000), Diffused Reflectance Spectrophotometer(DRS), and Horiba make (Model: Fluoromax-4C\_1379D\_2015, Photoluminescence(PL) spectrophotometer respectively. The detailed structural properties and the phase composition of the samples were done with Transmission Electron Microscopy(TEM) using an FEI FP 5022 transmission electron microscope. The elemental analysis of the sample was done with X-ray Photoelectron Spectroscopy(XPS) using Nexa Base (Thermofisher Scientific) X-ray photoelectron spectrophotometer(Al,  $K_{\alpha}$  source).

#### 2.3.2. Photoelectrochemical measurements

Photoelectrochemical (PEC) measurements were carried out using an electrochemical workstation (Mode: PGSTAT-302, Make: Metrohm-Autolab) with a three-electrode system with Ag/AgCl and platinum foil employed as the reference and counter electrodes, respectively. A solution of 0.1 M KCl containing 0.01 M  $\text{K}_3[\text{Fe}(\text{CN})_6]$  was used as the supporting electrolyte for electrochemical impedance spectroscopy (EIS) scanning, and the frequency range was from 100 kHz to 0.01 Hz at an amplitude of

10 mV. The water oxidation studies were understood from the Linear sweep voltammetry (LSV) analyses of the samples. An aqueous NaOH (1 M) was used as the electrolyte for LSV and the scanning was performed at 100 mV/s scan rate with potential applied between -0.9 to 0.9 V vs. Ag/AgCl in dark conditions. The irradiated analyses were conducted using a 100 mW/cm<sup>2</sup> tungsten halogen lamp with an AM 1.5G filter. All the PEC measurements were carried out at room temperature(25 °C). The samples were coated ( $1 \times 1 \text{ cm}^2$ ) with fluorine-doped tin oxide and used as the working electrode.

### 2.4. Computational methods

Initially, a self-consistent field (SCF) convergence test was performed to obtain cutoff kinetic energy (50 Ry), charge density (275 Ry) and k-mesh ( $6 \times 6 \times 3$ ). Using this setting we have optimized the  $2 \times 2 \times 1$  supercell structure of anatase  $\text{TiO}_2$  ( $[(\text{TiO}_2)_{16}]$ , tetragonal, space group: I41/amd (141)) and rutile  $\text{TiO}_2$  ( $[(\text{TiO}_2)_8]$ , tetragonal, space group: P42/mnm (136)). In this step, the crystal structures were fully relaxed (vc-relax) using the BFGS algorithm implemented in Quantum ESPRESSO until the forces converged below  $10^{-3}$  Ry/Bohr. Besides, the convergence threshold for electronic optimization was  $10^{-6}$  Ry, and the fermi-dirac occupation method is employed with a smearing width of 0.01 Ry. Similarly, “vc-relax” calculations were repeated for Fe-substituted  $\text{TiO}_2$  structures before the electronic structure calculations. Further, the optimized structures were used for the electronic structure calculations. The electronic band dispersion curve was obtained along high symmetry points. As for the density of states calculations, the k-point was  $6 \times 6 \times 3$ , and the fermi-dirac occupation method was employed for both structures.

### 2.5. Photocatalytic experimental setup

The photocatalytic experiment was conducted in batch mode under conditions of natural sunlight (intensity:700 W/m<sup>2</sup>) and

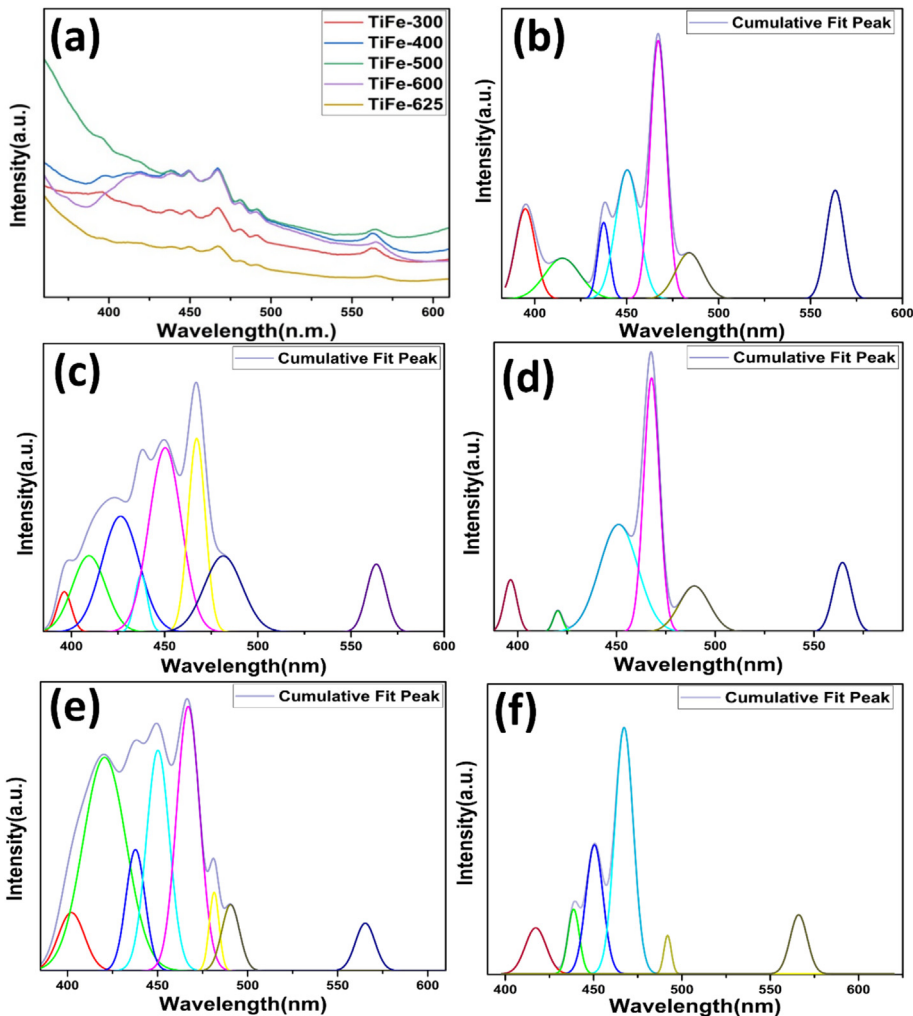


**Fig. 4.** (a)PL spectra and deconvoluted peaks of (b)TiFe-300,(c)TiFe-400, (d)TiFe-500, (e)TiFe-600 and (f)TiFe-625.

visible light (Source: Philips LED, 100 W/m<sup>2</sup>). The light intensity was measured using a radiometer (International Light Tech., ILT2400) and the photon flux for the visible light source was found to be  $1.05 \times 10^{20}$  photons/sec. The probe pollutants were Methylene blue(0.01 mM) and metanil yellow(0.01 mM). An amount of 0.5 g/L catalyst was dispersed in a 30 ml pollutant solution. The samples were collected at regular intervals of 10 min for 60 min. The sacrificial agents used for scavenger testing were iso-propyl alcohol (hole scavenger), EDTA (hydroxyl scavenger) and Benzoquinone (super-oxide scavenger).

### 3. Result and discussion

**Fig. 1(a and b)** depicts the X-ray diffraction (XRD) patterns of the pristine and Fe-doped mixed-phase TiO<sub>2</sub> samples. Anatase and rutile peaks in the patterns were identified by comparing them with the standard database (JCPDS Card Nos. 89-4203, 89-4920) and were marked accordingly. The undoped TiO<sub>2</sub> calcined at different temperatures showed that the anatase to rutile phase transformation starts at 500 °C, and the rutile phase suppresses the anatase phase as the temperature increases. Interestingly, the anatase phase completely disappeared once the calcination temperature reached 700 °C. On the other hand, according to XRD patterns shown in **Fig. 1(b)**, the Fe-doped TiO<sub>2</sub> samples calcined at different temperatures do not exhibit impurity peaks due to their low doping content, indicating a successful incorporation of the dopants

into the crystal lattice. By comparing the two XRD patterns, it is observed that the onset temperature required for phase transformation of doped TiO<sub>2</sub> has reduced significantly to 400 °C, while for undoped TiO<sub>2</sub>, it is 500 °C. In other words, the transition temperature of phase transformation is lowered with the Fe doping. This could be because anatase has a more stable equilibrium at low temperatures but collapses with the increase in temperature. Consequently, Ti-O bonds are broken and reorganised into octahedrals to generate a rutile phase [23]. The partial phase transformation at optimum temperature and beyond may be due to the growth of smaller-sized particles to large particles before transforming to rutile that would have utilised additional time and temperature to form a complete rutile phase, as reported by Ding et al. [9]. The samples' crystallite size and anatase–rutile (A/R) ratios were calculated using the Debye-Scherrer and the Spurr formula, respectively and given in **Table 1** [24,25]. It can be seen that the phase transformation leads to an increase in crystallite size in the doped samples. As we gradually increase the temperature to achieve a high A/R ratio TiO<sub>2</sub>, the grain boundary defects reduce and cause an apparent increase in crystallite size [26].

The surface morphology of undoped and Fe-doped TiO<sub>2</sub> is shown in **Fig. 2(a and b)**. At first glance, the surface morphology of doped TiO<sub>2</sub> is almost identical to that of undoped one, which could be due to the addition of very low Fe concentration. The doped sample is calcined further to form the mixed phase TiO<sub>2</sub>, and interestingly, it was observed that an increase in calcination temperature did not result in morphology variation in the samples

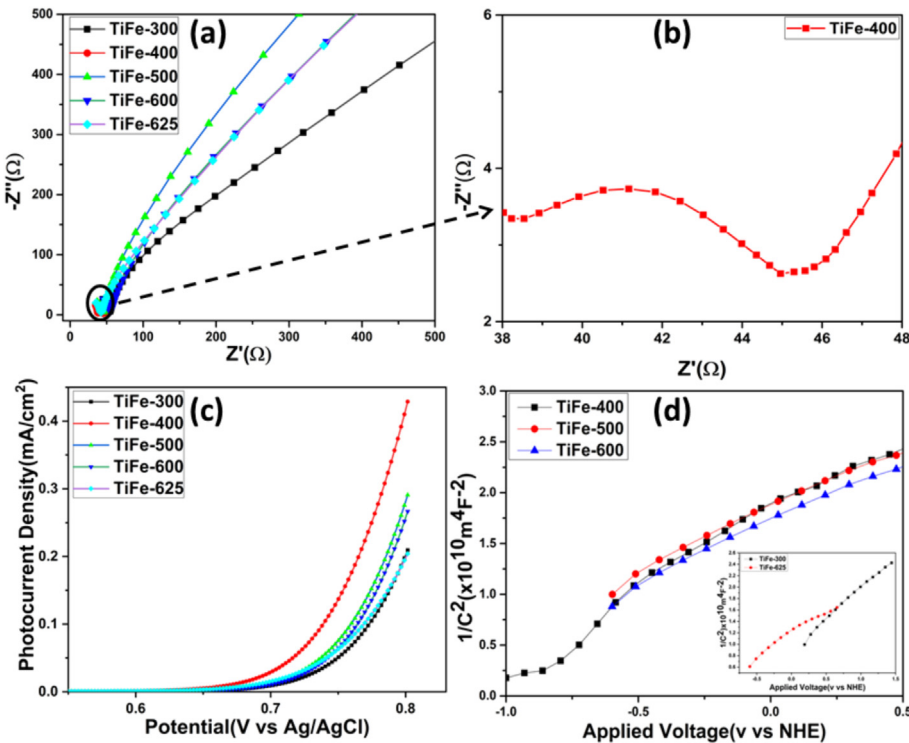


**Fig. 5.** (a-b) Nyquist plot, (c) LSV plot and (d) Mott-Schottky plot of the samples.

(See Figure S2). A closer look at the FESEM image of TiFe-300 (Figure SI 1(a)) reveals the granular structure on the surface that is absent in the other samples calcined at higher temperatures. This could be because TiFe-300 has less crystallinity, as seen in the XRD pattern, and the enhanced crystallinity of the samples through calcination led to the removal of granular structures from the samples. The energy dispersive spectrum (EDS) of the Fe-doped  $\text{TiO}_2$  samples confirmed the successful doping (Figure S3).

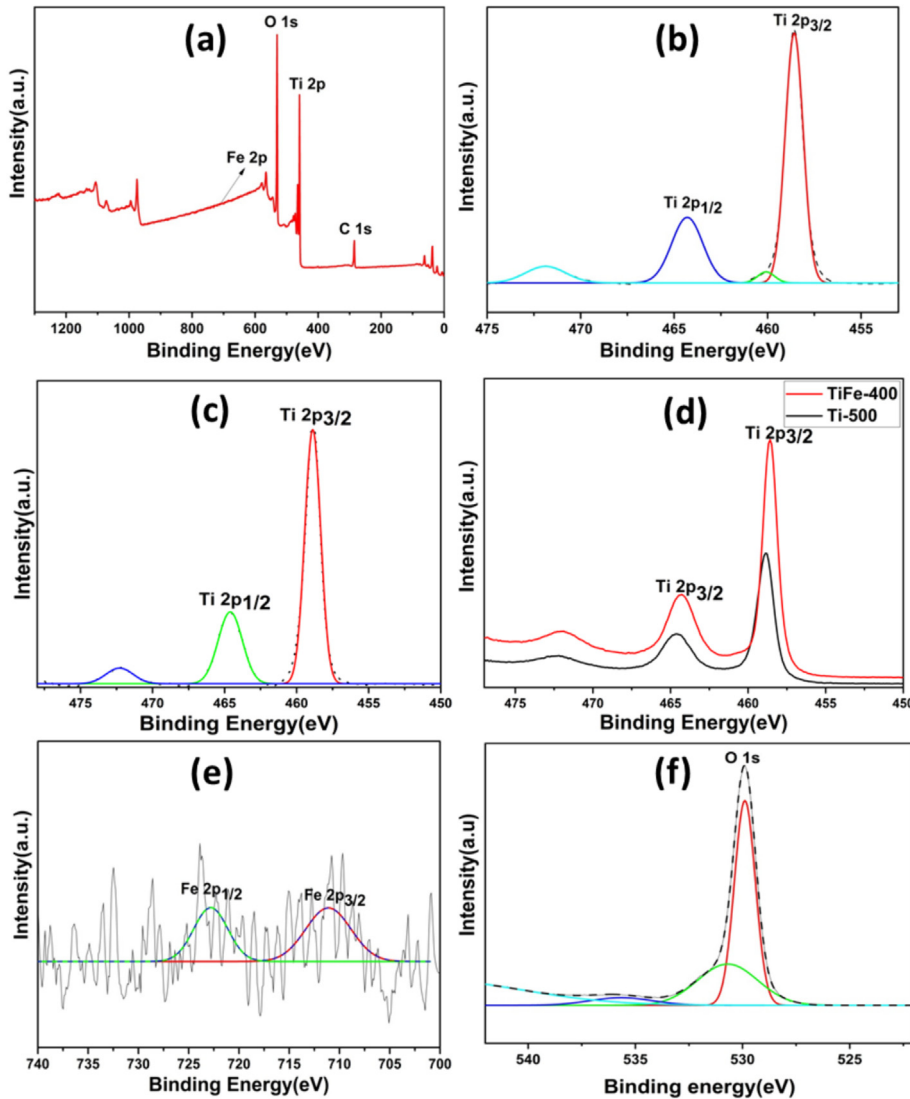
To further investigate the structure and junction formation of mixed-phase  $\text{TiO}_2$ , the TEM and HRTEM images of TiFe-400 are given in Fig. 2(c-f). Referring to Fig. 2(c), it can be seen that TiFe-400 consists of nanoparticles with a narrow size distribution as implied from the particle size distribution histogram (Fig. 2 (d)), and many particles appear to be connected through linking points. The formation of heterojunction due to the presence of these linking points are evident in Fig. 2(e), along with the markings. The interplanar distance of the formed heterojunctions was calculated from the HRTEM image (Fig. 2(f)). It was consistent with the (004) plane of anatase and (011) plane of the rutile phase, respectively. The mixed-phase nature of the sample was further confirmed by the SAED (Fig. 2(g)) with the patterns indexed as anatase (013) and rutile (140). The TEM and HRTEM result confirms the co-existence of the anatase and rutile phases and is in accordance with the XRD result.

Fig. 3(a and b) shows absorbance spectra obtained from the UV-Vis DRS analyses. As shown in Fig. 3(a), the role of Fe doping in improving the light absorption capacity of the doped samples is evident from the sharp cut-off wavelengths above 400 nm exhibited by the doped samples, corresponding to the bandgap of  $\sim 2.9$  eV.

Further, it is observed that the absorption spectra shift towards the visible region with the increase in the rutile content. The shifting of the absorption towards the higher wavelength can be attributed to the electron excitations from Fe-3d states to the  $\text{TiO}_2$  conduction band [27]. The band gap energies of the sample were

determined from Tauc's plot (Fig. 3(b)) and given in Table 2. All the doped samples' bandgap was lower than the undoped  $\text{TiO}_2$  sample. Doping introduces new energy levels between the valence and conduction bands, reducing bandgap energy [28]. From the absorption spectral studies, it can be inferred that a synergy of doping and mixed-phase formation can cause a shift in the absorption spectra towards the visible region. The reduced bandgap of the Fe-doped  $\text{TiO}_2$  could be due to the strong electronic and chemical interactions between Fe and  $\text{TiO}_2$ , which can be further confirmed by DFT calculations reported in the later section.

The PL spectra of the Fe-modified  $\text{TiO}_2$  with varying phase ratios are given in Fig. 4(a). The PL intensity was highest for Fe-doped mixed-phase  $\text{TiO}_2$  samples and lowest for the TiFe-300 and TiFe-625. The charge separation dynamics of the samples were studied using the intensity of the photoluminescence spectroscopy. All the mixed-phase  $\text{TiO}_2$  obtained at different calcination temperatures were found to have relatively high PL intensities. On the other hand, the low PL intensity in the case of TiFe-300 and TiFe-625 may be because, unlike other samples which have mixed phase  $\text{TiO}_2$ , TiFe-300 and TiFe-625 have single phase (anatase or rutile). Moreover, traditional Type-II heterojunction is expected to have low PL intensity via reduced charge carrier recombination, but Z-scheme heterojunction exhibits a modified charge transfer process. Hence, the high PL intensity of TiFe-400, TiFe-500 and TiFe-600 could be due to the Z-scheme heterojunction formation between anatase-rutile mixed phase, which is missing in TiFe-300 and TiFe-625. This increased PL intensity can be ascribed to the electron migration from anatase to rutile as per the Z-scheme mechanism, resulting in charge carrier recombination on the rutile phase. As a result, holes remain intact on the VB of anatase and electrons on the CB of rutile [29]. The deconvoluted PL emission peaks are shown in Fig. 4(b-f). The peaks around 400 nm are due to the band-edge emission arising from the band-to-band electron-hole recombination, and the 415 nm and 468 nm are due to the shallow trap states closer to the conduction band. Among the emission



**Fig. 6.** (a) XPS survey spectra, (b) High resolution Ti 2p spectra of TiFe-400, (c) High resolution Ti 2p spectra of Ti-500, (d) comparison of Ti 2p spectra of TiFe-400 and Ti-500 (e) High resolution Fe 2p spectra of TiFe-400, (d) High resolution O 1s spectra of TiFe-400.

peaks due to trap states, the peak around 425 nm is due to the self-trapped excitons localised on  $\text{TiO}_6$  octahedral. In contrast, the peak at 438 nm is due to the relaxation of self-trapped excitons generated through the band edge transitions [30]. The peak of about 468 nm is due to the charge transfer transition for an electron trapped by an oxygen vacancy [31].

EIS was used to study the charge separation process at the semiconductor/electrolyte interface of the samples. Nyquist plots of the samples under illumination are given in Fig. 5(a) and (b) shows an enlarged Nyquist plot of TiFe-400. The Nyquist plot consists of a semicircle arc indicative of the charge transfer resistance ( $R_{ct}$ ) at the semiconductor ( $\text{TiO}_2$ )/electrolyte interface, and a smaller arc radius (i.e. smaller  $R_{ct}$  value) indicates low charge transfer resistance [19]. The obtained  $R_{ct}$  values are given in Table 2. TiFe-400 exhibits the lowest  $R_{ct}$  value among all the photoelectrodes. This decrease can be attributed to the formation of anatase-rutile heterojunction in TiFe-400, which improves the electron transfer rate. Further, it can also be observed that with the increase in the rutile content in the doped mixed samples, the  $R_{ct}$  value is increasing, and the highest  $R_{ct}$  is noticed for TiFe-625. This is due to the narrowing of the conduction pathways from the rutile to anatase through which the electron transfer occurs. As the rutile content

increases, the anatase nanoparticles get surrounded by more rutile nanoparticles, which are non-conducting. This reduces the conduction pathways and thus hinders efficient electron transport [32,33]. The lowest  $R_{ct}$  obtained for TiFe-400 indicates efficient charge separation and transport, therefore making it an optimal photoactive material.

The photoelectrochemical water oxidation capability of the samples is examined from the LSV analysis under illuminated conditions (Fig. 5(c)). The photocurrent curves indicate the water oxidation due to the photo-generated holes [34]. Among all the samples, the photocurrent densities of the mixed-phase  $\text{TiO}_2$  samples were higher. This can be attributed to better charge separation and transport in the mixed-phase samples. Mainly, the TiFe-400 sample exhibits the highest photocurrent at low overpotential (0.43 mA/cm<sup>2</sup>, potential V vs Ag/AgCl), almost twice that of other samples, indicating superior water splitting ability. The reduced overpotential and high photocurrent values of the optimal sample indicate the existence of energetically suitable properties for water-splitting applications. This can be ascribed to the synergistic effect of Fe doping and optimised phase ratio in the direct Z-scheme  $\text{TiO}_2$ . The Fe dopants in the  $\text{TiO}_2$  lattice inhibit charge recombination by acting as trap centres. Further, forming a direct

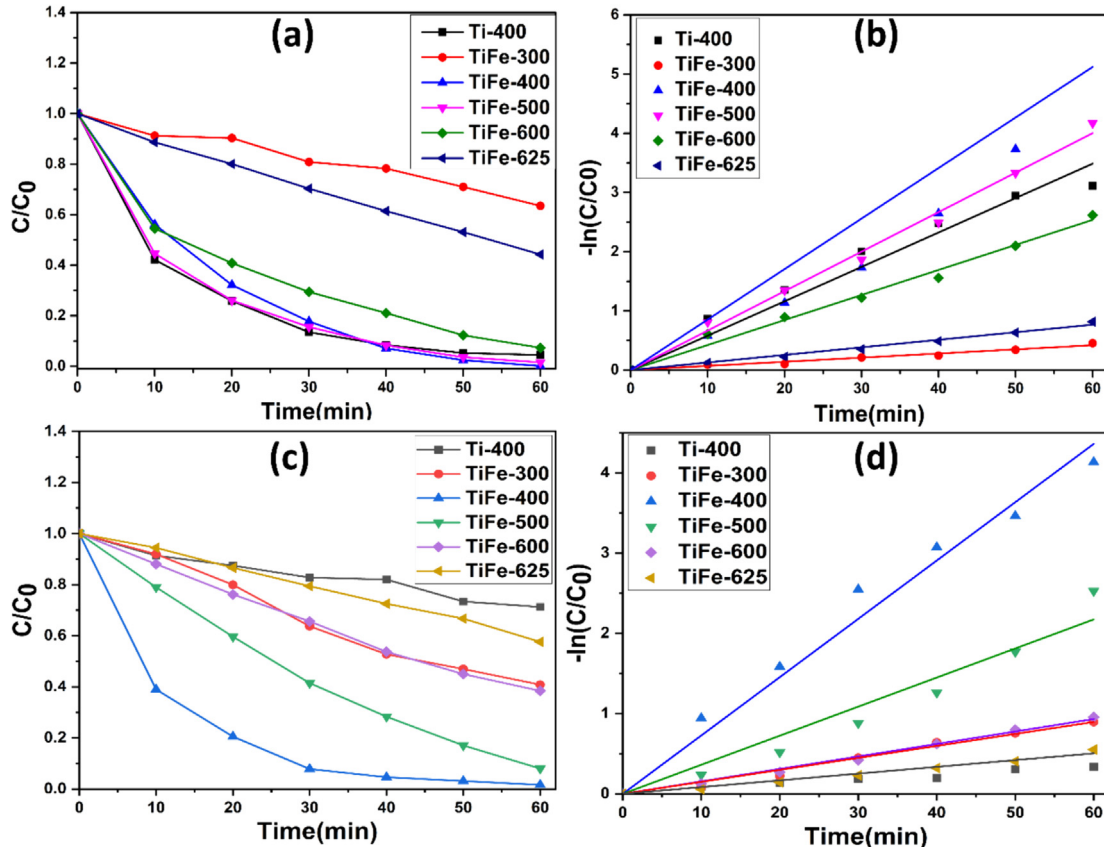


**Fig. 7.** (a)  $C/C_0$  vs Time, (b) rate constant for methylene blue, (c)  $C/C_0$  vs Time, (d) rate constant plots of metanil yellow under solar irradiation. (For interpretation of the references to colour in this figure legend, the reader is referred to the web version of this article.)

Z-scheme in the optimal sample allowed better charge transportation due to conduction pathways [35]. Additionally, as observed from the PL spectrum, higher oxygen vacancies in the TiFe-400 sample can also factor in the improved photocurrent response [36]. The comparative study demonstrating the formation of a direct Z-scheme, which is responsible for enhancing water-splitting performance, is explained using a systematic radical trapping test in the later section.

Mott-Schottky(M–S) studies of the samples were performed to further understand the electronic properties of the samples. The M–S plots are depicted in Fig. 5(d) from which the flat band potential was determined using the equation:

$$\frac{1}{C^2} = \left[ \frac{2}{\epsilon \in_0 eN} \right] \left[ E - V_{fb} - \frac{kT}{e} \right]$$

[37]. The  $V_{fb}$  of the samples TiFe-300, TiFe-400, TiFe-500, TiFe-600 and TiFe-625 are  $-0.33$  V,  $-0.81$  V,  $-0.47$  V,  $-0.49$  V and  $-0.48$  V respectively. The TiFe-400 sample shows a greater shift towards negative potential indicating to the accumulation of electrons in the material [38]. The low  $R_{ct}$  and high photocurrent density indicate the higher electron concentration in TiFe-400. Studies have shown that the conduction band minimum ( $E_{CB}$ ) is approximately  $0.1$  V negative than the  $V_{fb}$  [39]. Considering this, the  $E_{CB}$  of TiFe-400 (Anatase) is  $-0.91$  eV(vs NHE). The valence band minimum ( $E_{VB}$ ) is related to  $E_{CB}$  via the relation:-  $E_{VB} = E_{CB} + E_g$ , where  $E_g$  is the band gap. Using this relation, the  $E_{VB}$  for TiFe-400 is found to be  $2.03$  eV.

The elemental analysis and binding energies of Ti, Fe, and O in the TiFe-400 sample were determined from XPS spectra. The survey spectra (Fig. 6(a)) confirm the presence of Ti, Fe, O and C on

the TiFE-400 surface. The C 1s peak results from the organic precursors used in the sol-gel synthesis method. The High-resolution XPS spectrum of Ti is given in Fig. 6(b). The deconvoluted spectra revealed four peaks:  $Ti^{4+}$  ( $Ti\ 2p_{3/2}$ ) at  $458.6$  eV,  $Ti^{4+}$  ( $Ti\ 2p_{1/2}$ ) at  $464.3$  eV,  $Ti^{3+}$  ( $Ti\ 2p_{3/2}$ ) at  $460.1$  eV and  $Ti^{3+}$  ( $Ti\ 2p_{1/2}$ ) at  $471.8$  eV [40]. The two minor peaks indicating the existence of  $Ti^{3+}$  are due to the oxygen vacancy in the lattice and are consistent with the PL studies. To further understand the influence of Fe doping, the Ti 2p spectra of TiFe-400 are compared with Ti 2p spectra of undoped mixed phase  $TiO_2$ -Ti-500 (Fig. 6(c-d)). A close inspection reveals a negative shifting of  $Ti\ 2p_{3/2}$  peaks of TiFe-400 compared to Ti-500, indicating electron transfer from Fe species to  $TiO_2$  [41,42]. The presence of oxygen vacancies confirmed from the PL and XPS studies indicates that oxygen vacancies are one of the dominant defects in the material. The  $Fe\ 2p_{3/2}$  and  $Fe\ 2p_{1/2}$  are located at  $711.1$  eV and  $722.7$  eV, respectively (Fig. 6(e)). The Fe peaks  $711.08$  and  $722.74$  indicate the presence of  $Fe^{2+}$  (- $Fe\ 2p_{3/2}$  and  $Fe\ 2p_{1/2}$ , respectively) [22,41]. The low doping concentration of Fe is evident from the weak signal of Fe 2p peaks. The main O 1s peak at  $529.8$  eV (Fig. 6(f)) confirms the lattice oxygen in  $TiO_2$ . Further, the shoulder peak and peak at the higher binding energy indicate significant surface hydroxyl groups or chemisorbed water molecules [43].

The photocatalytic performance of the samples was understood by studying the photodegradation of probe pollutants: methylene blue and metanil yellow. The photodecomposition activity was carried out under visible and solar light irradiation. The photocatalytic degradation kinetics were understood from the  $C/C_0$  vs time graph, where  $C$  is solution concentration at time  $t$ ,  $C_0$  is initial concentration and were found to be following Langmuir –Hinshelwood kinetics. Further, the rate constants for the sample were

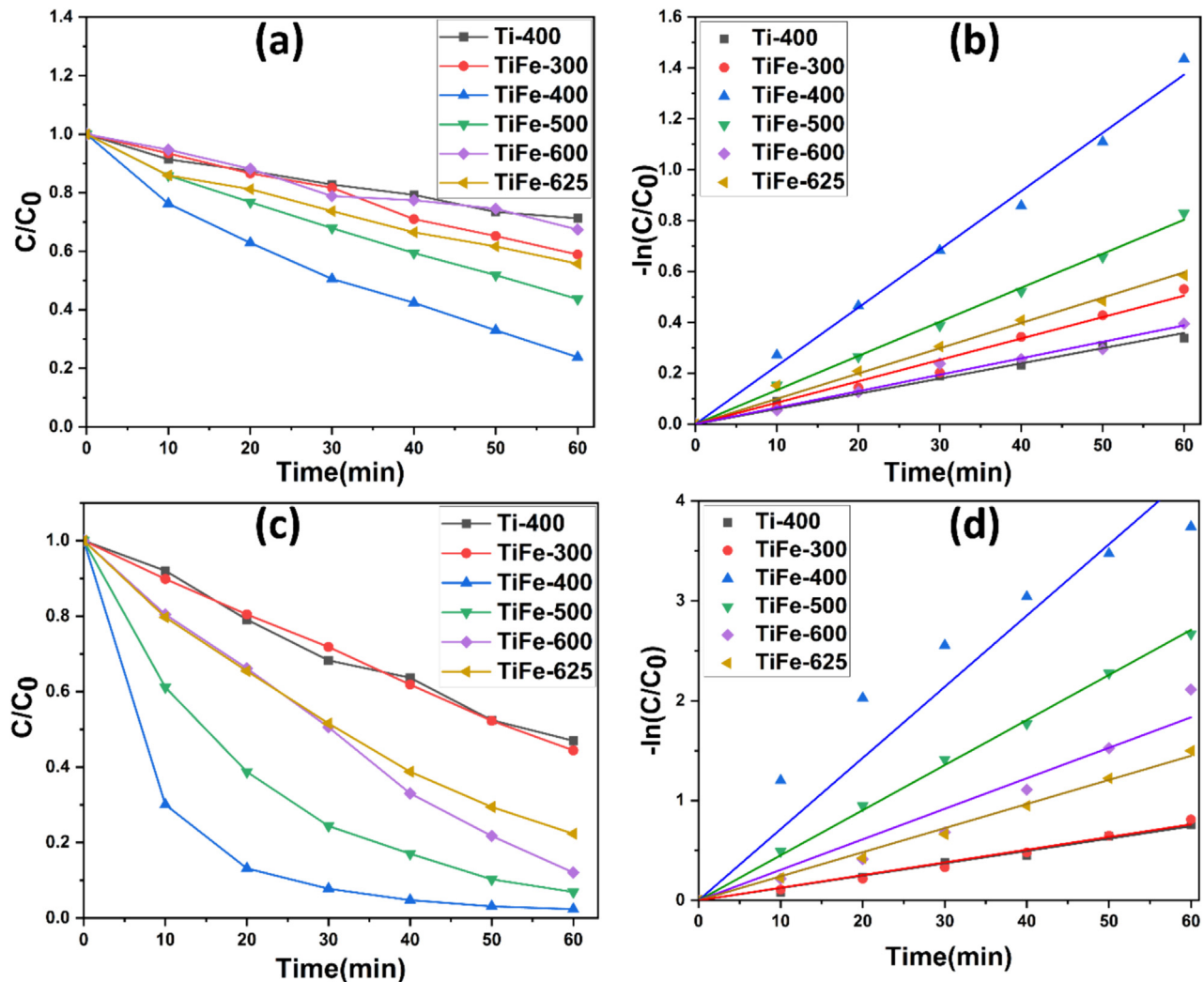


**Fig. 8.** (a)  $C/C_0$  vs Time, (b) rate constant for methylene blue, (c)  $C/C_0$  vs Time, (d) rate constant plots of metanil yellow under visible irradiation. (For interpretation of the references to colour in this figure legend, the reader is referred to the web version of this article.)

determined using the pseudo-first-order kinetic equation:  $\ln(C/C_0) = -kt$ , where  $k$  is the rate constant. The solar photocatalytic degradation kinetics for both pollutants are given in Fig. 7(a-d), whereas the visible light degradation kinetics for the pollutants are given in Fig. 8(a-d).

The calculated rate constant values of the samples for both the pollutants under the two irradiation conditions are given in Table 2.

As expected, mixed-phase  $\text{TiO}_2$  samples showed higher photocatalytic performance in visible and solar illumination conditions than undoped and doped single-phase  $\text{TiO}_2$ . The low photocatalytic performance of single-phase  $\text{TiO}_2$  (TiFe-300 and TiFe-625) can be attributed to the unfavourable crystallographic properties, poor charge transport mechanism and high charge carrier recombination. One might be compelled to draw a conclusion that the low PL intensity of TiFe-300 and TiFe-625 is an indication of suppressed charge recombination. However, the low crystalline nature of TiFe-300 and the NIR region emission due to the presence of 100 % rutile content in TiFe-625 may have contributed to the PL intensity [44,45]. Also, as explained before, the higher PL intensity may hint at the formation of Z-scheme heterojunction in the samples. Further, it can be noted that the performance of mixed-phase samples is better under solar irradiation compared to the visible irradiation

condition. Under visible light illumination, the rutile phase acts as the major source for photo-generated electrons due to its lower bandgap energy. Whereas under the solar illumination condition both anatase and rutile phase acts as the source of photo-generated electrons. Among all the mixed-phase samples, the photocatalytic activity of TiFe-400, having 60 % anatase (1.48A/R ratio), was the highest. As obtained from the electrochemical studies, TiFe-400 showed a low charge transfer resistance and a higher concentration of electrons that facilitate the photoactivity of the optimal sample. On the other hand, the PL results suggest a formation of direct Z-scheme in mixed-phase  $\text{TiO}_2$ , which may have assisted the practical separation of photoinduced charge carriers and might have assisted the dye degradation at a prompt rate. Additionally, the trap levels identified from PL analyses due to doping also suppress the charge carrier recombination process and create an electron surplus. The trend in performance in terms of rate constant decreases with the increase in the rutile content in the mixed-phase sample. This can be either because of the formation of more trap levels in anatase than in rutile or because the trap levels in rutile act as recombination centres. In either case, it can be concluded that a phase dependency on optimal direct Z-scheme/Type-II heterojunction is visible. The reusability of the best performing sample-TiFe-400 was evaluated by a stability test

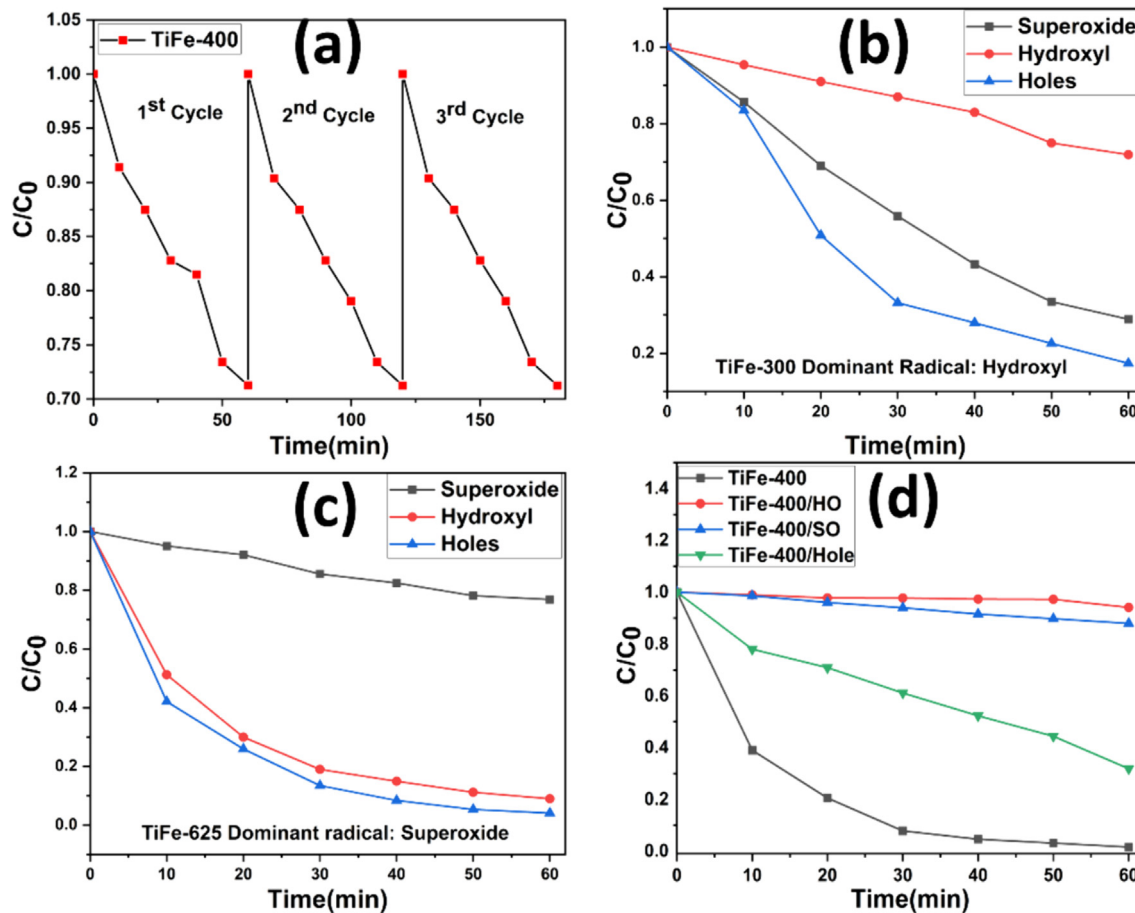


Fig. 9. (a)Stability Test of TiFe-400, Radical trapping tests of (b) TiFe-300 (c)TiFe-625 (d)TiFe-400 and (e).

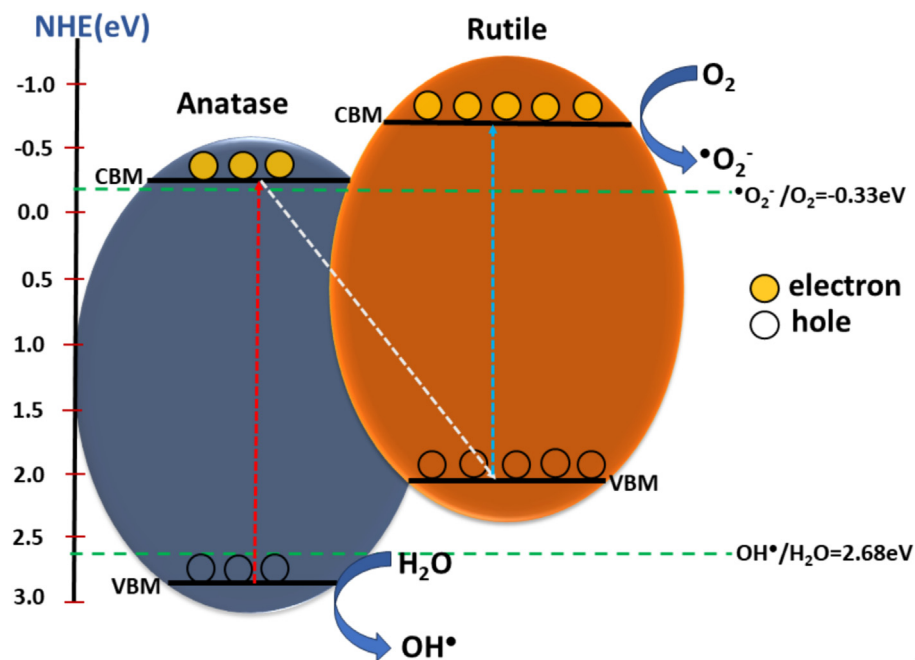
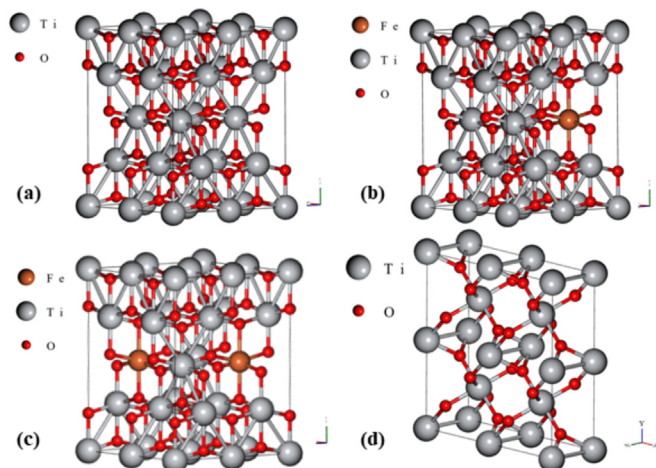


Fig. 10. Schematic diagram of the proposed mechanism.



**Fig. 11.** The relaxed structures of (a) pure anatase TiO<sub>2</sub>, (b) 1-Fe doped TiO<sub>2</sub>, (c) 2-Fe doped TiO<sub>2</sub> and (d) pure rutile TiO<sub>2</sub>.

under solar irradiation conditions (Fig. 9(a)). After testing 03 cycles, the photocatalytic performance did not diminish, indicating the reusability and stability of the sample.

To understand the type of heterojunction formed, radical trapping tests for the samples TiFe-300, TiFe-625 and TiFe-400 with metanil yellow as probe pollutant using hydroxyl(OH·), superoxide(O<sub>2</sub><sup>-</sup>) and hole scavenger were performed under solar irradiation. It is observed from Fig. 9(b) and (c) that OH· and O<sub>2</sub><sup>-</sup> are the dominant radicals species in TiFe-300 and TiFe-625 samples, respectively. As Fig. 9(d) shows, OH· and O<sub>2</sub><sup>-</sup> are dominating radical species contributing to the TiFe-400 photocatalysis process. According to the traditional view regarding charge transfer happening in mixed-phase TiO<sub>2</sub>, the electrons flow from the rutile to the anatase phase, and holes migrate from the anatase to the rutile phase to participate in the photocatalytic process. But as obtained from M-S analysis, the valence band position(vs NHE) is at 2.03 eV, which is more negative VB edge potential than the standard redox potential of OH<sup>-</sup>/H<sub>2</sub>O pair thus eliminating the possibility of OH<sup>-</sup> species from rutile phase playing a significant role in the photocatalytic degradation process. Instead of explaining the charge transfer by treating the semiconductor as Type II, it can be observed that the above contradiction can be well explained if the semiconductor is treated as a direct Z-scheme heterojunction. Here, the photogenerated holes in the anatase are retained in the VB. In contrast, the photogenerated electrons in the CB of anatase migrate to the VB of rutile and thus recombine with the holes. This leaves behind electrons in rutile CB and holes in anatase VB, preventing further recombination. The electron in the rutile CB having a potential of -0.90 eV(vs NHE) can proceed further in reducing O<sub>2</sub><sup>-</sup> and the holes in anatase VB, obviously more positive than the standard redox potential of OH<sup>-</sup>/H<sub>2</sub>O pair, oxidizing H<sub>2</sub>O to OH<sup>-</sup>

radicals. To confirm the argument in the present work that the holes from the anatase phase and electrons from the rutile phase take part in the photocatalytic process, as opposed to the traditional view, the result of the radical trapping test of TiFe-400 can be compared with that of TiFe-300(anatase) and TiFe-625(rutile). It can be seen that for the TiFe-300(anatase phase) the hydroxyl radical is prominent species in the photocatalytic process, while it superoxide radical for the TiFe-625(rutile). This confirms our argument that in the case of TiFe-400, the photocatalytic process proceeds via a direct-Z scheme heterojunction formation. The holes from the anatase phase further carry on the photocatalytic degradation of dyes and water oxidation. Based on the mechanism explanation, a schematic diagram of the proposed mechanism is given in Fig. 10.

The influence of Fe atoms in the crystal lattice of anatase TiO<sub>2</sub> is analysed by comparing the DFT calculation with our experimental results. The 2 × 2 × 1 supercell structure of anatase TiO<sub>2</sub>, the Fe-doped structures and rutile TiO<sub>2</sub> are displayed in Fig. 11 (a-d). The DFT structure optimization of pure anatase TiO<sub>2</sub> yielded lattice parameters similar to our experimental values and consistent with previous reports, as given in Table 2 [46]. Further, it can be observed that the Fe- substitutional doping resulted in the reduction of lattice parameters. Besides, introducing the Fe atom in the crystal structure of anatase TiO<sub>2</sub> leads to an increase in the total energy per unit volume (E/V), matching with the E/V value of rutile TiO<sub>2</sub>. The DFT calculated total energies for the undoped (anatase and rutile) and doped TiO<sub>2</sub> are given in Table 3. It is noted that the total energy of TiO<sub>2</sub> (anatase, -5.378 eV) decreases with the addition of Fe atoms (-5.885 eV) and matches with the total energy of TiO<sub>2</sub> (rutile, -5.776 eV), which indicates that the Fe doping may assist in the anatase to rutile phase transformation. Moreover, the lower total energy of TiO<sub>2</sub> under Fe doping implies that the incorporation of Fe is thermodynamically favorable to form the rutile phase. Meanwhile, the decrease in cell volume of Fe-doped TiO<sub>2</sub> calculated from DFT (shown in Table 3) is another evidence of the thermodynamically driven force of doping-induced phase transformation, which mainly claims that the smaller cell volume can quickly transform to a rutile phase at low onset temperature [45].

Further, the electronic band structure and density of states (DOS) of pure anatase TiO<sub>2</sub>, 1/2 Fe atoms incorporated anatase TiO<sub>2</sub> and pure rutile TiO<sub>2</sub> structure are presented in Fig. 12 (a-d). The band structure of pure anatase TiO<sub>2</sub> along the high symmetry direction in the Brillouin zone, displayed in Fig. 12 (a), suggests an indirect band gap of 2.1 eV with the valence band maximum in the  $\Gamma$ M direction and conduction band minimum at the  $\Gamma$ - point. This underestimation as compared to the experimentally observed band gap of 3.4 eV is due to the approximations in the pseudopotentials and exchange-correlation functional considered in the current calculations [47,49,50]. However, other computationally demanding hybrid functionals, like HSE06, can be used to obtain more accurate band gap values [48,51]. Our calculations reveal that

**Table 3**  
The structural parameters obtained from the DFT calculations.

<b>Crystal system (2 × 2 × 1 supercell)</b>	<b>Lattice parameters</b>		<b>c/a ratio</b>	<b>Volume (Å<sup>3</sup>)</b>	<b>Total energy/volume (Ry/Å<sup>3</sup>)</b>
	<b>a = b (Å)</b>	<b>c (Å)</b>			
<b>Pure TiO<sub>2</sub> (anatase)</b>	Experimental [46]	7.592	9.444	1.243	544.336
	DFT [47]	7.600	9.700	1.276	560.272
	DFT [48]	7.636	9.747	1.276	568.32
	Our DFT	7.565	9.615	1.291	550.25
	Our experiment	7.556	9.470	1.253	540.671
<b>1 Fe – doped</b>		7.442	9.283	1.247	-5.885
<b>2 Fe – doped</b>		7.386	9.057	1.226	-5.750
<b>Pure TiO<sub>2</sub> (rutile)</b>		9.289	2.969	0.319	-5.776

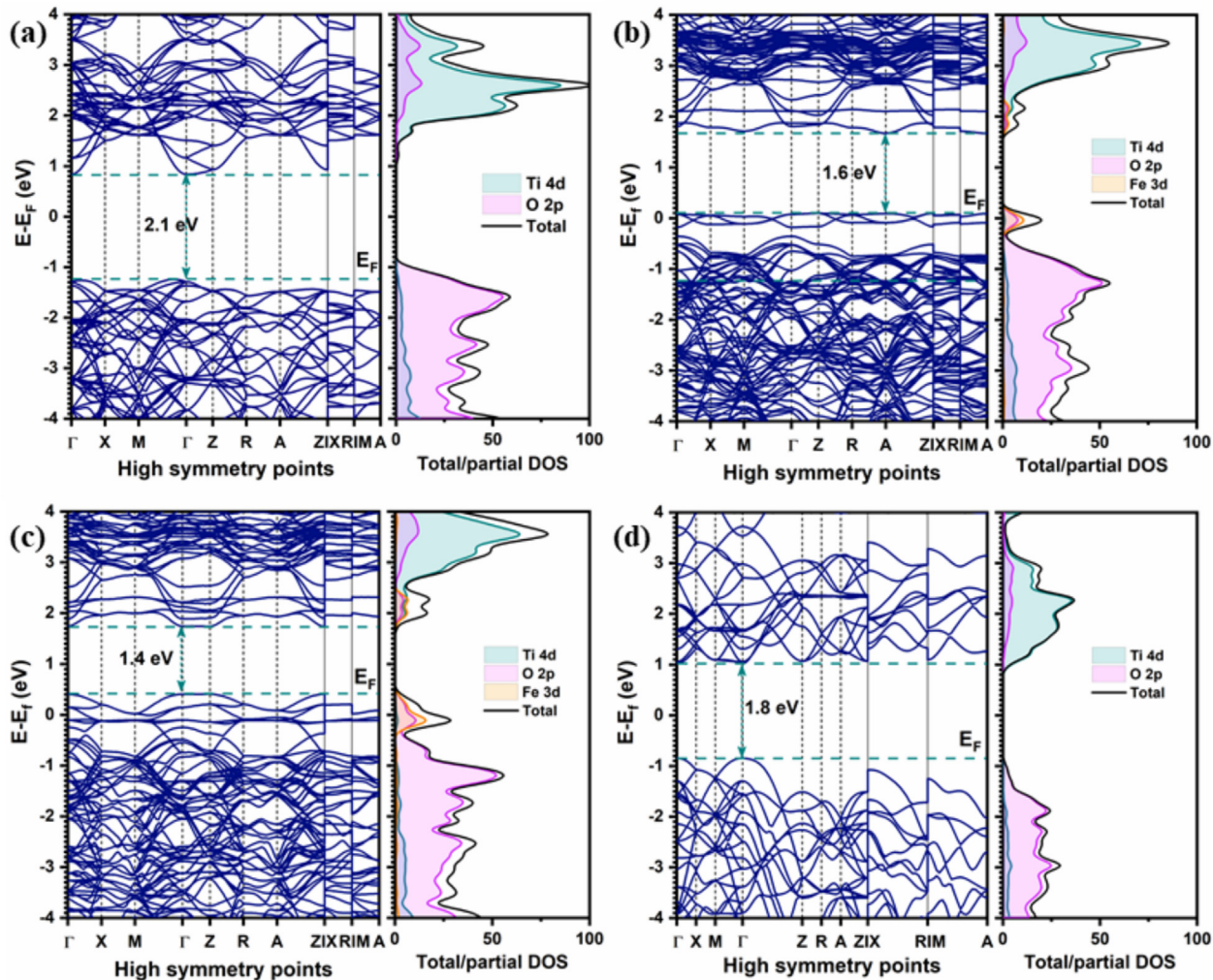


**Fig. 12.** Electronic band structures and corresponding density of states of (a) pure anatase  $\text{TiO}_2$ , (b, c) Fe incorporated systems and (d) pure rutile  $\text{TiO}_2$ .

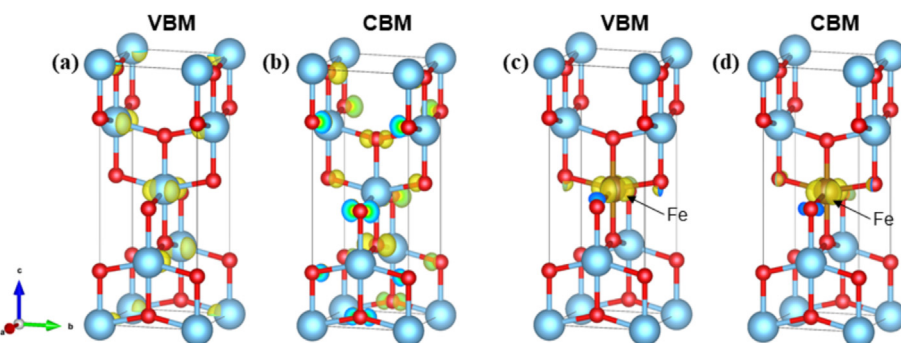


**Fig. 13.** The partial charge density distribution plots of the (a)&(b) pure  $\text{a}-\text{TiO}_2$  and (c)&(d)  $\text{a}-\text{TiO}_2$  with Fe atom (iso value = 0.007).

the incorporation of the Fe atom in the  $\text{TiO}_2$  structure results in the formation of additional bands below the conduction band minimum and above the valence band maximum. These Fe-induced sub-bands reduce the band gap from 2.1 eV to 1.6 (for 1 Fe atom) and 1.4 eV (for 2 Fe atoms). Besides, their flat nature indicates a higher probability of direct band-to-band transitions than rutile  $\text{TiO}_2$  (Fig. 12(d)). These DFT results confirm the role of Fe atoms in the reduction of band gap values which is in good agreement with our experimental observations. Our calculations reveal that the incorporation of the Fe atom in the  $\text{TiO}_2$  structure results in

the formation of additional bands below the conduction band minimum and above the valence band maximum. These Fe-induced sub-bands as seen in figures lead to the reduction of the computed band gap from 2.1 eV to 1.6 (1 Fe atom) and 1.4 eV (2 Fe atoms) as well as their flat nature might increase the probability of direct band-to-band transitions. Thus, the findings confirm the influence of Fe atoms on the reduction in band gap, as observed in our experiments. As a result, the performance of the optimal doped sample in photocatalytic and photoelectrochemical reactions enhanced. Both experimental and theoretical results further claim that the

contribution of Fe to the forbidden gap of  $\text{TiO}_2$  leads to reduced charge carrier recombination. Besides, the band structure of rutile  $\text{TiO}_2$  suggests a direct band gap of 1.8 eV along the  $\Gamma$ -symmetry point. The corresponding density of states (DOS), as seen in Fig. 12, reveals that the major contribution to the VBM consists of O 2p states and the CBM consists of antibonding Ti 4d orbitals. The perturbations arising from the magnetic Fe atoms may have led to the spin-orbit coupling and splitting of bands, resulting in the significant reduction in band gap by 0.5 eV with the pure anatase  $\text{TiO}_2$ . The corresponding DOS of pure anatase  $\text{TiO}_2$  reveals that the major contribution to the VBM consists of O 2p states, and the CBM consists of antibonding Ti 4d orbitals. The perturbations arising from the doped Fe atoms may have led to the splitting of bands, creating additional Fe 3d states and a significant band gap reduction. As a result, the photoactivity of the doped samples in photocatalytic and photoelectrochemical reactions is enhanced.

The postprocessing of the bands corresponding to the valence band maximum and conduction band minimum at the respective k-points provides further insights into the charge density distribution and thus their participation in the bonding. The charge density plots of pure  $\text{a-TiO}_2$  and Fe substituted structures, displayed in Fig. 13 (a-d), reveal the strong contribution of Fe 3d orbitals to the VBM. This modified charge density may be responsible for the enhanced photocatalytic activity in Fe-doped  $\text{TiO}_2$ .

#### 4. Conclusion

Direct Z-scheme-based low onset temperature mixed phase anatase/rutile  $\text{TiO}_2$  was obtained by using minimal Fe doping and followed by the calcination. The characteristics of a direct Z-scheme heterojunction can be attributed to the formation of biphasic  $\text{TiO}_2$  during calcination. Fe doping results in the transformation of anatase  $\text{TiO}_2$  to rutile  $\text{TiO}_2$  at low onset temperature (400 °C). Designed direct Z-scheme mixed phase  $\text{Fe-TiO}_2$  to enhance the photocatalytic and PEC performance is of great importance from both theoretical and experimental standpoints. Fe atoms triggered the anatase-to-rutile phase transformation by virtue of low crystal size and cell volume calculated from experimental and DFT studies.  $\text{Fe-TiO}_2$  sample calcined at 400 °C has about 40 % rutile phase and 60 % anatase phase, exhibiting the highest photocatalytic and PEC performance. The optimal material with Fe doping exhibits better light absorption capacity in the visible range, consistent with the observation of band gap narrowing due to Fe doping in DFT studies. The enhanced visible-light-driven photoactivity of optimal mixed phase (anatase/rutile)  $\text{Fe-TiO}_2$  was attributed to the formation of the direct Z-scheme-based charge transfer route, which is different from the traditional type-II heterojunction mechanism and confirmed from the systematic radical trapping test. These unique and simple approaches will be helpful to design efficient photoactive materials for future use.

#### CRediT authorship contribution statement

**S.K. Nikhil:** Writing – original draft, Resources, Methodology, Investigation, Formal analysis, Data curation. **Gopika Rajeev Nair:** Methodology, Data curation. **Abinash Das:** Validation, Resources. **Sebin Devasia:** Validation, Software, Formal analysis. **Ranjith G. Nair:** Writing – review & editing, Supervision, Project administration, Methodology, Formal analysis, Conceptualization.

#### Declaration of competing interest

The authors declare that they have no known competing financial interests or personal relationships that could have appeared to influence the work reported in this paper.

#### Acknowledgments

The authors gratefully acknowledge the fund received from the Department of Science and Technology, Government of India, through the DST-FIST project (SR/FST/PSI-212/2016(C)). The authors also sincerely thank the help received from MRC, MNIT Jaipur in FESEM analysis, AMRC, IIT Mandi in HRTEM, XPS analysis and Dr. M. Bhagavatachri, Department of Energy, Madras University (Guindy Campus) for photoelectrochemical analysis analyses.

#### Appendix A. Supplementary material

The Characterization methods including photoelectrochemical measurements and photocatalytic reaction setup, FESEM images and EDX micrographs are given in Supplementary Information provided along with the manuscript. Supplementary data to this article can be found online at <https://doi.org/10.1016/j.apt.2024.104683>.

#### References

- [1] A. Das, M.K. Adak, N. Mahata, B. Biswas, Wastewater treatment with the advent of  $\text{TiO}_2$  endowed photocatalysts and their reaction kinetics with scavenger effect, *J. Mol. Liq.* 338 (2021) 116479. <https://doi.org/10.1016/j.molliq.2021.116479>.
- [2] A. Das, Hierarchical  $\text{ZnO-TiO}_2$  nanoheterojunction. A strategy driven approach to boost the photocatalytic performance through the synergy of improved surface area and interfacial charge transport, *Appl. Surf. Sci.* (2020).
- [3] H.M. Mousa, J.F. Alenezi, I.M.A. Mohamed, A.S. Yasin, A.-F.-M. Hashem, A. Abdal-hay, Synthesis of  $\text{TiO}_2@ZnO$  heterojunction for dye photodegradation and wastewater treatment, *J. Alloy. Compd.* 886 (2021) 161169. <https://doi.org/10.1016/j.jallcom.2021.161169>.
- [4] S.B. Nair, K.A. John, J.A. Joseph, S. Babu, V.K. Shinoj, S.K. Remillard, S. Shaji, R.R. Philip, Fabrication and characterization of Type-II heterostructure n: In 2 O 3 / p:in-TiO 2 for enhanced photocatalytic activity, *Phys. Status Solidi (b)* 258 (2021). <https://doi.org/10.1002/pssb.202000441>.
- [5] S. Al Jitan, G. Palmisano, C. Garlisi, Synthesis and surface modification of  $\text{TiO}_2$ -based photocatalysts for the conversion of CO<sub>2</sub>, *Catalysts* 10 (2020) 227. <https://doi.org/10.3390/catal10020227>.
- [6] D.O. Scanlon, C.W. Dunnill, J. Buckeridge, S.A. Shevlin, A.J. Logsdail, S.M. Woodley, C.R.A. Catlow, M. Powell, R.G. Palgrave, I.P. Parkin, A.A. Sokol, Band alignment of rutile and anatase  $\text{TiO}_2$ , *Nat. Mater.* (2013). <https://doi.org/10.1038/nmat3697>.
- [7] H. Sutiono, A.M. Tripathi, H.-M. Chen, C.-H. Chen, W.-N. Su, L.-Y. Chen, H. Dai, B.-J. Hwang, Facile synthesis of [101]-oriented rutile  $\text{TiO}_2$  nanorod array on FTO substrate with a tunable anatase-rutile heterojunction for efficient solar water splitting, *ACS Sustain. Chem. Eng.* 4 (2016) 5963–5971. <https://doi.org/10.1021/acssuschemeng.6b01066>.
- [8] X. Zhang, J. Chen, S. Jiang, X. Zhang, F. Bi, Y. Yang, Y. Wang, Z. Wang, Enhanced photocatalytic degradation of gaseous toluene and liquidus tetracycline by anatase/rutile titanium dioxide with heterophase junction derived from materials of Institut Lavoisier-125(Ti): Degradation pathway and mechanism studies, *J. Colloid Interface Sci.* 588 (2021) 122–137. <https://doi.org/10.1016/j.jcis.2020.12.042>.
- [9] L. Ding, S. Yang, Z. Liang, X. Qian, X. Chen, H. Cui, J. Tian,  $\text{TiO}_2$  nanobelts with anatase/rutile heterophase junctions for highly efficient photocatalytic overall water splitting, *J. Colloid Interface Sci.* 567 (2020) 181–189. <https://doi.org/10.1016/j.jcis.2020.02.014>.
- [10] D. Salazar-Marín, G. Oza, J.A.D. Real, A. Cervantes-Uribe, H. Pérez-Vidal, M.K. Kesrala, J.G.T. Torres, S. Godavarthi, Distinguishing between type II and S-scheme heterojunction materials: a comprehensive review, *Appl. Surface Sci. Adv.* 19 (2024) 100536. <https://doi.org/10.1016/j.apsadv.2023.100536>.
- [11] Y. Duan, L. Liang, K. Lv, Q. Li, M. Li,  $\text{TiO}_2$  faceted nanocrystals on the nanofibers: Homojunction  $\text{TiO}_2$  based Z-scheme photocatalyst for air purification, *Appl. Surf. Sci.* 456 (2018) 817–826. <https://doi.org/10.1016/j.apsusc.2018.06.128>.
- [12] F. Xu, W. Xiao, B. Cheng, J. Yu, Direct Z-scheme anatase/rutile bi-phase nanocomposite  $\text{TiO}_2$  nanofiber photocatalyst with enhanced photocatalytic H<sub>2</sub>-production activity, *Int. J. Hydrogen Energy* 39 (2014) 15394–15402. <https://doi.org/10.1016/j.ijhydene.2014.07.166>.
- [13] Y. Yuan, R. Guo, L. Hong, X. Ji, Z. Lin, Z. Li, W. Pan, A review of metal oxide-based Z-scheme heterojunction photocatalysts: actualities and developments, *Mater. Today Energy* 21 (2021) 100829. <https://doi.org/10.1016/j.mtener.2021.100829>.
- [14] R. Medhi, M.D. Marquez, T.R. Lee, Visible-light-active doped metal oxide nanoparticles: review of their synthesis, properties, and applications, *ACS Appl. Nano Mater.* 3 (2020) 6156–6185. <https://doi.org/10.1021/acsnm.oc01035>.
- [15] L. Kernazhitsky, V. Shymanovska, T. Gavrilko, V. Naumov, V. Kshnyakin, T. Khalyavka, A comparative study of optical absorption and photocatalytic

- properties of nanocrystalline single-phase anatase and rutile TiO<sub>2</sub> doped with transition metal cations, *J. Solid State Chem.* 198 (2013) 511–519. <https://doi.org/10.1016/j.jssc.2012.11.015>.
- [16] C. Wang, Z. Chen, H. Jin, C. Cao, J. Li, Z. Mi, Enhancing visible-light photoelectrochemical water splitting through transition-metal doped TiO<sub>2</sub> nanorod arrays, *J. Mater. Chem. A* 2 (2014) 17820–17827. <https://doi.org/10.1039/C4TA04254A>.
- [17] V. Soni, A.N. Singh, P. Singh, A. Gupta, Photocatalytic dye-degradation activity of nano-crystalline Ti 1-x M x O 2-δ (M =Ag, Pd, Fe, Ni and x = 0, 0.01) for water pollution abatement, *RSC Adv.* 12 (2022) 18794–18805. <https://doi.org/10.1039/D2RA02847F>.
- [18] A. Singh, S. Kumari, R. Shrivastav, S. Dass, V. Satsangi, Iron doped nanostructured TiO<sub>2</sub> for photoelectrochemical generation of hydrogen, *Int. J. Hydrogen Energy* 33 (2008) 5363–5368. <https://doi.org/10.1016/j.ijhydene.2008.07.041>.
- [19] W. Chakhar, Fe-doped TiO<sub>2</sub> nanorods with enhanced electrochemical properties as efficient photoanode materials, *J. Alloy. Compd.* (2017).
- [20] G.K. Sukhadeve, S.Y. Janbandhu, R. Kumar, D.H. Lataye, D.D. Ramteke, R.S. Gedam, Visible light assisted photocatalytic degradation of Indigo Carmine dye and NO<sub>2</sub> removal by Fe doped TiO<sub>2</sub> nanoparticles, *Ceram. Int.* 48 (2022) 29121–29135. <https://doi.org/10.1016/j.ceramint.2022.05.053>.
- [21] M. Zhou, J. Yu, B. Cheng, Effects of Fe-doping on the photocatalytic activity of mesoporous TiO<sub>2</sub> powders prepared by an ultrasonic method, *J. Hazard. Mater.* 137 (2006) 1838–1847. <https://doi.org/10.1016/j.jhazmat.2006.05.028>.
- [22] S.K. Nikhil, G.R. Nair, M. Kumar, M. Bhagavathiachari, R.G. Nair, A doped heterojunction photoanode: a strategy-driven approach to improve the charge carrier dynamics and photoconversion performance of the TiO<sub>2</sub>-based dye-sensitized solar cell, *J Mater Sci: Mater Electron* 35 (2024) 602. <https://doi.org/10.1007/s10854-024-12344-7>.
- [23] P.P. Sarnagan, A. Lakshmanan, D. Sarkar, Influence of anatase-rutile ratio on band edge position and defect states of TiO<sub>2</sub> homojunction catalyst, *Chemosphere* 286 (2022) 131692. <https://doi.org/10.1016/j.chemosphere.2021.131692>.
- [24] M. Izzi, M.C. Sportelli, L. Torsi, R.A. Picca, N. Cioffi, Synthesis and antimicrobial applications of ZnO nanostructures: a review, *ACS Appl. Nano Mater.* 6 (2023) 10881–10902. <https://doi.org/10.1021/acsanm.3c01432>.
- [25] R.A. Spurr, Howard. Myers, Quantitative analysis of anatase-rutile mixtures with an X-Ray diffractometer, *Anal. Chem.* 29 (1957) 760–762. <https://doi.org/10.1021/ac60125a006>.
- [26] R.S. Dubey, Temperature-dependent phase transformation of TiO<sub>2</sub> nanoparticles synthesized by sol-gel method, *Mater. Lett.* 215 (2018) 312–317. <https://doi.org/10.1016/j.matlet.2017.12.120>.
- [27] M. Einert, P. Hartmann, B. Smarsly, T. Brezesinski, Quasi-homogenous photocatalysis of quantum-sized Fe-doped TiO<sub>2</sub> in optically transparent aqueous dispersions, *Sci. Rep.* 11 (2021) 17687. <https://doi.org/10.1038/s41598-021-96911-6>.
- [28] S. Ahadi, N.S. Moalej, S. Sheibani, Characteristics and photocatalytic behavior of Fe and Cu doped TiO<sub>2</sub> prepared by combined sol-gel and mechanical alloying, *Solid State Sci.* 96 (2019) 105975. <https://doi.org/10.1016/j.solidstatesciences.2019.105975>.
- [29] J. He, Y. Du, Y. Bai, J. An, X. Cai, Y. Chen, P. Wang, X. Yang, Q. Feng, Facile formation of anatase/rutile TiO<sub>2</sub> nanocomposites with enhanced photocatalytic activity, *Molecules* 24 (2019) 2996. <https://doi.org/10.3390/molecules24162996>.
- [30] D. Komaraiah, E. Radha, N. Kalarikkal, J. Sivakumar, M.V. Ramana Reddy, R. Sayanna, Structural, optical and photoluminescence studies of sol-gel synthesized pure and iron doped TiO<sub>2</sub> photocatalysts, *Ceram. Int.* 45 (2019) 25060–25068. <https://doi.org/10.1016/j.ceramint.2019.03.170>.
- [31] G. Xu, Y. Zhang, D. Peng, D. Sheng, Y. Tian, D. Ma, Y. Zhang, Nitrogen-doped mixed-phase TiO<sub>2</sub> with controllable phase junction as superior visible-light photocatalyst for selective oxidation of cyclohexane, *Appl. Surface Sci.* 536 (2021) 147953. <https://doi.org/10.1016/j.apsusc.2020.147953>.
- [32] D.C. Hurum, A.G. Agrios, K.A. Gray, T. Rajh, M.C. Thurnauer, Explaining the enhanced photocatalytic activity of degussa P25 Mixed-phase TiO<sub>2</sub> using EPR, *J. Phys. Chem. B* 107 (2003) 4545–4549. <https://doi.org/10.1021/jp0273934>.
- [33] R.R. Guimarães, A.L.A. Parussulo, H.E. Toma, K. Araki, Enlightening the synergic effect of anatase/rutile mixtures in solar cells, *Electrochim. Acta* 188 (2016) 523–528. <https://doi.org/10.1016/j.electacta.2015.12.040>.
- [34] A. Das, T. Deka, P.M. Kumar, M. Bhagavathiachari, R.G. Nair, Ag-modified ZnO nanorods and its dual application in visible light-driven photoelectrochemical water oxidation and photocatalytic dye degradation: a correlation between optical and electrochemical properties, *Adv. Powder Technol.* 33 (2022) 103434.
- [35] K.M. Chahrour, F.K. Yam, A.M. Eid, Water-splitting properties of bi-phased TiO<sub>2</sub> nanotube arrays subjected to high-temperature annealing, *Ceram. Int.* 46 (2020) 21471–21481. <https://doi.org/10.1016/j.ceramint.2020.05.246>.
- [36] H. Pai, T.-R. Kuo, R.-J. Chung, S. Kubendhiran, S. Yougbaré, L.-Y. Lin, Enhanced photocurrent density for photoelectrochemical catalyzing water oxidation using novel W-doped BiVO<sub>4</sub> and metal organic framework composites, *J. Colloid Interface Sci.* 624 (2022) 515–526. <https://doi.org/10.1016/j.jcis.2022.05.169>.
- [37] F. Spadavecchia, G. Cappelletti, S. Ardizzone, M. Ceotto, L. Falchiola, Electronic structure of pure and N-doped TiO<sub>2</sub> nanocrystals by electrochemical experiments and first principles calculations, *J. Phys. Chem. C* 115 (2011) 6381–6391. <https://doi.org/10.1021/jp2003968>.
- [38] J. Bandara, U.W. Pradeep, Tuning of the flat-band potentials of nanocrystalline TiO<sub>2</sub> and SnO<sub>2</sub> particles with an outer-shell MgO layer, *Thin Solid Films* 517 (2008) 952–956. <https://doi.org/10.1016/j.tsf.2008.07.031>.
- [39] J.H. Kim, A. Ma, H. Jung, H.Y. Kim, H.R. Choe, Y.H. Kim, K.M. Nam, In situ growth of the Bi<sub>2</sub>3 nanowire array on the Bi<sub>2</sub>Mo<sub>6</sub> film for an improved photoelectrochemical performance, *ACS Omega* 4 (2019) 17359–17365. <https://doi.org/10.1021/acsomega.9b02111>.
- [40] P. Makal, D. Das, Self-doped TiO<sub>2</sub> nanowires in TiO<sub>2</sub>-B single phase, TiO<sub>2</sub>-B/anatase and TiO<sub>2</sub>-anatase/rutile heterojunctions demonstrating individual superiority in photocatalytic activity under visible and UV light, *Appl. Surf. Sci.* 455 (2018) 1106–1115. <https://doi.org/10.1016/j.apsusc.2018.06.055>.
- [41] N. Kanjana, W. Maiangree, P. Poolcharuansin, P. Laokul, Synthesis and characterization of Fe-doped TiO<sub>2</sub> hollow spheres for dye-sensitized solar cell applications, *Mater. Sci. Eng. B* 271 (2021) 115311. <https://doi.org/10.1016/j.mseb.2021.115311>.
- [42] G. Cheng, X. Liu, X. Song, X. Chen, W. Dai, R. Yuan, X. Fu, Visible-light-driven deep oxidation of NO over Fe doped TiO<sub>2</sub> catalyst: Synergic effect of Fe and oxygen vacancies, *Appl. Catal. B* 277 (2020) 119196. <https://doi.org/10.1016/j.apcatb.2020.119196>.
- [43] V. Moradi, M.B.G. Jun, A. Blackburn, R.A. Herring, Significant improvement in visible light photocatalytic activity of Fe doped TiO<sub>2</sub> using an acid treatment process, *Appl. Surf. Sci.* 427 (2018) 791–799. <https://doi.org/10.1016/j.apsusc.2017.09.017>.
- [44] Y.F. You, C.H. Xu, S.S. Xu, S. Cao, J.P. Wang, Y.B. Huang, S.Q. Shi, Structural characterization and optical property of TiO<sub>2</sub> powders prepared by the sol-gel method, *Ceram. Int.* 40 (2014) 8659–8666. <https://doi.org/10.1016/j.ceramint.2014.01.083>.
- [45] B. Anitha, M.A. Khadar, Anatase-rutile phase transformation and photocatalysis in peroxide gel route prepared TiO<sub>2</sub> nanocrystals: Role of defect states, *Solid State Sci.* 108 (2020) 106392. <https://doi.org/10.1016/j.jsolidstatesciences.2020.106392>.
- [46] M. Horn, C.F. Schwebdtfeger, E.P. Meagher, Refinement of the structure of anatase at several temperatures, *Zeitschrift Für Kristallographie - Crystalline Materials* 136 (1972) 273–281. <https://doi.org/10.1524/zkri.1972.136.16.273>.
- [47] C. H. Park, S. B. Zhang and S.-H. Wei, Phys. Rev. B: Condens. Matter Mater. Phys., 2002, 66, 73202 – Google Search, (n.d.). <https://www.google.com/search?q=C.+H.+Park%2C+S.+B.+Zhang+and+S.-H.+Wei%2C+Phys.+Rev.+B%3A+Condens.+Matter+Mater.+Phys.%2C+2002%2C+66%2C+73202&oq=C.+H.+Park%2C+S.+B.+Zhang+and+S.-H.+Wei%2C+Phys.+Rev.+B%3A+Condens.+Matter+Mater.+Phys.%2C+2002%2C+66%2C+73202&aq=chrome,.69i57.1161j0j15&sourceid=chrome&ie=UTF-8> (accessed October 11, 2021).
- [48] Hybrid Functional Study on Electronic and Optical Properties of the Dopants in Anatase TiO<sub>2</sub>, (n.d.). <https://pubs.acs.org/doi/epdf/10.1021/acsomega.3c04329> (accessed January 26, 2024).
- [49] H. Hamad, M.M. Elsenety, W. Sadik, A.-G. El-Demerdash, A. Nashed, A. Mostafa, S. Elyamny, The superior photocatalytic performance and DFT insights of S-scheme CuO@TiO<sub>2</sub> heterojunction composites for simultaneous degradation of organics, *Sci. Rep.* 12 (2022) 2217. <https://doi.org/10.1038/s41598-022-05981-7>.
- [50] J.S. Lin, W.-C. Chou, S.-Y. Lu, G.-J. Jang, B.-R. Tseng, Y.-T. Li, Density functional study of the interfacial electron transfer pathway for monolayer-adsorbed InN on the TiO<sub>2</sub> Anatase (101) surface, *J. Phys. Chem. B* 110 (2006) 23460–23466. <https://doi.org/10.1021/jp061975u>.
- [51] Y. Wang, H. Zhang, P. Liu, X. Yao, H. Zhao, Engineering the band gap of bare titanium dioxide materials for visible-light activity: a theoretical prediction, *RSC Adv.* 3 (2013) 8777. <https://doi.org/10.1039/c3ra40239h>.